1	Do upper-plate material properties or fault frictional properties play			
2	more important roles in tsunami earthquake characteristics?			
3				
4	Qingjun Meng ¹ , Benchun Duan ^{1*}			
5				
6	(1) Center of Tectonophysics, Department of Geology & Geophysics, Texas A&M University			
7	College Station, TX, United States.			
8	Corresponding author: Benchun Duan (<u>bduan@tamu.edu</u>)			

Abstract

10

11

12

13

14

15

16

17

18

19

20

21

22

23

24

25

26

27

28

29

30

31

Tsunami earthquakes are a type of shallow subduction zone events that rupture slowly (<1.5 km/s) with exceptionally long duration and depleted high frequency radiation, resulting in a large discrepancy of Mw and Ms magnitudes and abnormally large tsunami along coastal areas. Heterogeneous fault frictional properties at shallow depth have been thought to dominate tsunami earthquake generation. Some recent studies propose heterogeneous upper-plate material properties determine rupture behavior of megathrust earthquakes, including characteristics of tsunami earthquakes. In this study, we use a recently developed 3D dynamic earthquake simulator to explore tsunami earthquake generation and systematically examine roles of upper-plate material properties and fault frictional properties in tsunami earthquake characteristics in a physics-based framework. For heterogeneous fault friction, we consider isolated asperities with strongly velocity-weakening properties embedded in a conditionally stable zone with weakly velocity-weakening properties. For heterogeneous upper-plate properties, we consider a generic depth profile of seismic velocity and rigidity constrained from seismic surveys. We design a set of models to explore their effects on tsunami earthquake generation and characteristics. We find that the conditionally stable zone can significantly slow down rupture speeds of earthquakes that nucleate on asperities to be < 1.5 km/s over a large depth range (1-20 km), while heterogeneous upper-plate properties can only reduce rupture speeds to be ~1.5-2.0 km/s over a narrow depth range (1-3km). Nevertheless, heterogeneous upper-plate properties promote cascading rupture over multiple isolated asperities on the shallow subduction plane, contributing to large tsunami earthquake generation. We also find that fault frictional properties play much more important roles than upper-plate material properties in long normalized duration, high-frequency depletion and low moment-scaled radiated energy in tsunami earthquakes. In addition, the effective normal stress on the subduction plane, which affects fault frictional strength, also influences the characteristics of tsunami earthquakes, including duration, stress drop and moment-scaled radiated energy.

Keywords: tsunami earthquakes, fault friction, upper-plate material, effective normal stress, rupture speed, normalized duration, moment-scaled radiated energy

1. Introduction

Tsunami earthquakes are interplate earthquakes along shallow subduction zones that generate much larger tsunami than that their surface wave magnitude (*Ms*) implies (Kanamori, 1972). There have been a number of well-studied tsunami earthquakes, including the 1992 Nicaragua earthquake (Kanamori and Kikuchi, 1993), the 1994 Java earthquake (Abercrombie *et al.*, 2001; Bilek and Engdahl, 2007), the 1996 Peru earthquake (Ihmlé *et al.*, 1998), the 2006 Java earthquake (Ammon *et al.*, 2006; Bilek and Engdahl, 2007), and the 2010 Mentawai earthquake (Lay *et al.*, 2011), listed in Table S1 together with some earlier events. Compared to ordinary earthquakes, tsunami earthquakes have slow rupture speeds around 1.5 km/s or slower, abnormally long duration (e.g., 185 s for Java 2006 event), source spectra depleted in short-period energy, resulting in large discrepancy between their *Ms* and *Mw* magnitudes (e.g., *Ms* 7.2 vs *Mw* 7.8 for Java 2006 event), and low moment-scaled radiated energy. They usually occur along the shallow portion (e.g., < 15 km depth) of subduction interfaces.

A conceptual model based on the rate- and state-dependent fault friction has been proposed to understand tsunami earthquake generation. For example, Bilek and Lay (2002) studied both large tsunami earthquakes and smaller shallow subduction zone earthquakes and found that they all have longer normalized duration compared with deeper earthquakes (> 15km). They proposed that these earthquakes are associated with ruptures on locally locked unstable patches (asperities) within largely conditionally stable zones over shallow subduction interfaces. Frictional stability regimes over subduction interface are typically defined in the framework of the rate- and state-dependent friction law, including stable zones where fault slips stably without seismic radiation, unstable zones where seismic slip occurs, and conditionally stable zones where slip is generally stable but earthquakes can propagate through them at slow speeds (Scholz, 1998). Bilek and Lay (2002) proposed that the locally locked unstable patches may be related to subducted seamounts, ridges and host and graben structure, which could produce roughness on subduction zone interfaces. The conditionally stable zone could be a transition zone between the shallow velocity strengthening area (aseismic) and the downdip velocity weakening area (seismic). There are different mechanisms explaining this transition. Early studies proposed that the transition of smectite clays to illite and chlorite, when smectite gets dehydrated as temperature increases with depth, could trigger a change from velocity strengthening to velocity weakening (Wang, 1980; Hyndman and Wang, 1993; Hyandman et al., 1997). Saffer et al. (2012) proposed that mineral precipitation, for example calcite and quartz, and shear localization could function in driving the frictional transition and the heterogeneity of fault frictional behavior.

52

53

54

55

56

57

58

59

60

61

62

63

64

65

66

67

68

69

70

71

72

73

Recently, Sallares and Ranero (2019) proposed that, without the necessity to consider fault mechanics, depth-dependent upper-plate elastic properties determine depth-varying rupture

characteristics, including larger slip, slower rupture speed and depletion of high frequency energy for earthquakes at the shallow domain (depth< 5 km) than those at the deep domain (depth>10 km). Prada *et al.* (2021) performed 3D dynamic rupture modeling to assess the difference in rupture behaviors between the shallow and deep domains, adopting a slip-weakening law with essentially uniform fault friction properties on the fault plane. They concluded that a depth-dependent upper plate rigidity explains most of the observed seismological behaviors of both tsunami earthquakes and large megathrust earthquakes.

74

75

76

77

78

79

80

81

82

83

84

85

86

87

88

89

90

91

92

93

94

95

There are several concerns about the dominant role of the depth-dependent upper-plate property for tsunami earthquake generation advocated in these recent studies. First, without comparing roles of the upper-plate elastic property and the fault frictional property in one physics-based framework, it is premature to conclude which one plays a more important role in tsunami earthquake generation. Second, the rupture speed, which is typically lower than S wave velocity (Vs), is relatively small (~1.5 km/s) only at top 3 km depth, while below 5 km depth rupture speed is larger than 2 km/s (e.g., Figure 6e in Prada et al., 2021). This very narrow depth range (< 3 km) of slow rupture speed is not comparable to the observed range of centroid depth for historical tsunami earthquakes, which is up to 10 km (Bilek and Lay, 2002) or even to 15 km (Abercrombie et al., 2001). Complemental to the rupture speed, the normalized duration of earthquakes is a good measurement to compare duration of earthquakes of different sizes (Mw). Prada et al. (2021) did not calculate normalized durations of simulated earthquakes in their models and thus did not compare with those from observed tsunami earthquakes. Third, Prada et al. (2021) applied a 1D velocity structure constrained only for the upper plate from seismic data (Sallares and Ranero, 2019) to both the upper plate (hanging wall) and the under-thrusting plate (footwall) in their heterogeneous velocity model. They mainly compared this heterogeneous model to a homogeneous model to examine the dominant role of the upper-plate elastic property. When using a bimaterial model in which the 1D velocity structure in the hanging wall and a uniformly high velocity in the footwall are adopted, the rupture speed in their results (Figure 9c in Prada *et al.*, 2021) at shallow depth is much higher than that from their heterogeneous model, diminishing the effect of slowing down rupture by the upper-plate low-velocity layers at shallow depth.

96

97

98

99

100

101

102

103

104

105

106

107

108

109

110

111

112

113

114

115

116

117

In this study, we examine effects of the upper-plate elastic property and the fault frictional property on tsunami earthquake characteristics in one physics-based framework using a 3D fully dynamic earthquake simulator (Luo et al, 2020; Meng et al., 2022). We build a heterogeneous velocity structure model in which the upper-plate 1D velocity structure from Sallares and Ranero (2019) for the hanging wall is combined with a two-layer velocity structure for the footwall to examine roles of heterogeneous upper-plate elastic properties. For roles of the fault frictional property, we consider two asperities with strongly velocity-weakening friction properties, representing subducted seamounts, embedded in a conditionally stable zone with weakly velocityweakening friction properties on a shallow subduction interface. This heterogenous fault friction model is a simple case of the conceptual model for tsunami earthquake generation, in which strongly velocity-weakening asperities are embedded in a conditional stable friction environment (e.g., Bilek an Lay, 2002; Meng et al., 2022). Together with other models in which either simpler velocity structure or simpler friction distribution is adopted, we compare roles of heterogeneous upper-plate properties and heterogeneous fault friction properties in tsunami earthquake generation and characteristics. We examine rupture speeds, normalized duration, slip, stress drop and frequency contents from the models and compare them with those observed from historical tsunami earthquakes. We find that heterogeneous fault frictional properties play more important roles in tsunami earthquake generation and characteristics than heterogeneous upper-plate velocity structure.

120

121

122

123

124

125

126

127

128

129

130

131

132

133

134

135

136

137

138

118

119

2. Method

In this study, we use a fully dynamic earthquake simulator (Luo et al., 2020; Meng et al., 2022) to simulate slip behaviors of a shallow-dipping subduction interface over multiple earthquake cycles, including the coseismic, postseismic, interseismic, and nucleation phases. Unlike single-event dynamic rupture modeling, the multicycle dynamic simulations allow us to examine rupture characteristics of a sequence of dynamic events for a given set of model parameters. In particular, the initial stress condition for a dynamic event later in the sequence takes into account the effects of previous earthquake cycles, including previous dynamic events. The dynamic simulator is based on an explicit finite element method (FEM) code EQdyna that was developed for dynamic rupture simulations and has gone through multiple benchmark tests (Duan and Oglesby, 2006; Duan and Day, 2008; Duan, 2010; Duan, 2012; Luo and Duan, 2018; Liu and Duan, 2018). As a FEM method, the dynamic earthquake simulator can handle complex fault geometry (a shallow dipping subduction plane in this study) and heterogeneous velocity structure (upper-plate heterogeneous material properties). In addition, it captures spontaneously dynamic rupture propagation during the coseismic process of an earthquake cycle, while typical earthquake simulators such as RSQsim (Dieterich and Richards-Dinger, 2010) do not capture spontaneously dynamic rupture propagation. We remark that this type of 3D dynamic earthquake cycle modeling that includes the coseismic dynamic rupture process using a volumetric method such as FEM is computationally demanding. The dynamic earthquake simulator directly uses EQdyna to simulate coseismic dynamic processes, and integrates EQdyna with an adaptive dynamic relaxation technique (Qiang, 1988) and a variable time stepping scheme (Lapusta *et al.*, 2000) to simulate the quasi-static processes, including postseismic, interseismic, and nucleation phases. Thus, both dynamic and quasi-static processes are simulated within the same FEM framework. The quasi-static processes transition to dynamic processes when the maximum slip rate is larger than an empirical threshold V_{th1} =0.01 m/s, and the dynamic processes transition to quasi-static processes when the maximum slip rate is smaller than an empirical threshold value V_{th2} =0.005 m/s (Luo *et al.*, 2020; Meng *et al.*, 2022). On the plate interface, a commonly used rate-and state-dependent friction (RSF) law with aging law (Dieterich, 1979) is adopted (e.g., Lapusta *et al.*, 2000; Lapusta and Liu, 2009), as shown by equations:

149
$$\tau = \sigma * (f_0 + a \ln \frac{v}{v_0} + b \ln \frac{v_0 \theta}{L})$$
 (1)

$$\frac{d\theta}{dt} = 1 - \frac{v\theta}{L} \tag{2}$$

The friction strength τ is controlled by effective normal stress σ , reference friction coefficient f_0 , parameters a and b, slip rate V, reference slip rate V_0 , state variable θ and critical slip distance L. The friction strength, effective normal stress, slip rate and state variable will evolve through time automatically from their initial values based on equations (1)(2), while other parameters a, b, f_0 and L are fixed throughout multiple cycles. The friction strength is both rate dependent and state dependent, which is controlled by the friction parameters a and b. When a-b > 0, the fault plane is velocity strengthening and slip tends to be stable. When a-b < 0, the fault plane is velocity weakening, and slip can be either unstable or conditionally stable (Scholz, 1998; Liu and Rice, 2007), depending on the ratio of H/h*, where H is the fault width (the smaller dimension along strike and

dip) and h* is the critical nucleation size. When H is larger than h*, slip is unstable and earthquake can both nucleate and propagate. When H is equal or smaller than h*, slip is conditionally stable and earthquake can propagate but not nucleate in this zone. The critical nucleation size h* depends on multiple parameters, and an estimate of the nucleation size h* for 3D mode II earthquakes (Chen and Lapusta, 2009; Rubin and Ampuero, 2005) is:

$$h^* = \frac{\pi}{2} \frac{\mu b L}{(1 - \nu)(a - b)^2 \sigma} \tag{3}$$

where a, b, σ and L are the same parameters as in equation (1), ν is Poisson's ratio and μ is shear modulus.

3. Models

We set up 3D models with a dipping angle ϕ = 20° and the model dimension is shown in Figure 1a, with other basic parameters shown in Table S2. Because we focus on studying the shallow tsunami earthquakes, the main fault plane only extends to ~22 km in depth. The top boundary of the model is free surface (Z=0), while the left (X=Xmin) and right (X=Xmax) boundaries are fixed along X direction, $u_x = 0$. Other boundaries (Y=Ymin, Y=Ymax and Z=Zmin) are assigned with a loading rate of $0.5*V_{pl}$ =0.5x10° m/s parallel with the fault interface, to make the footwall to move downward and the hanging wall to move upward parallel with the fault plane. In these FEM models, we mainly use hexahedral elements for computation efficiency, while near the fault interface we cut a hexahedral element to two wedge elements to conform the shallow-dipping geometry, using the degeneration technique (Hughes, 2000; Duan, 2010; Duan, 2012; Luo and Duan, 2018). The thrust

fault intersects with free surface with a generally velocity weakening main fault plane surrounded by the velocity strengthening creeping area.

180

181

182

183

184

185

186

187

188

189

190

191

192

193

194

195

196

197

198

199

200

201

We design a set of models to systematically examine the effects of heterogeneous upper-plate velocity structure and heterogeneous fault friction on tsunami earthquake generation and characteristics. We have two velocity structure models (a simple model and a heterogeneous model) and two friction-distribution models (a uniform model and a nonuniform model). The simple velocity model applies two-layer velocity structure in both the hanging wall and footwall (Figure 1b). The two-layer structure, with a thin top layer overlying a half-space bottom layer, is a simplified structure of the upper part of subduction zone under-thrusting plate (Contreras-Reyes et al., 2017). The top layer (<2 km) has lower velocity Vp=5 km/s and Vs=2.5 km/s and the bottom layer has slightly higher velocity Vp=6.0 km/s and Vs=3.5km/s. The heterogeneous velocity model adopts the 1D depth-dependent velocity structure from Sallares and Ranero (2019) for the hanging wall and the two-layer structure for the footwall (Figure 1c). The 1D depth-dependent velocity structure is based on the upper-plate P-wave velocity obtained with travel-time modelling of seismic profiles across circum-Pacific and Indian Ocean subduction zones (Sallares and Ranero, 2019), within which the velocity and density at shallow depth drop significantly compared to those at deeper depth, implying a much more complaint prism than the simple velocity model. For the uniform friction model, the friction parameters a, b, critical distance, and effective normal stress are shown in Figure 2. Over most of the fault plane the a-b value is strongly velocity weakening with a value of -0.004, while a-b gradually increases from -0.004 at 4 km depth to 0.008 at the trench (Figure 2f). Friction parameter a-b also gradually increases to positive values on other three edges of the main fault plane (Figure 2c). We denote this friction distribution as the uniform friction model though friction

parameters are not strictly uniform on the main fault plane. The effective normal stress is 50 MPa below 4km depth (assuming overpressurization of pore fluid) and gradually reduces to 5 MPa near the trench (Figure 2g). The nonuniform friction model is designed based on the conceptual model for tsunami earthquake generation (e.g., Bilek and Lay, 2002; Meng et al., 2022), in which strongly velocity-weakening unstable asperities are embedded in a conditionally stable friction environment with weakly velocity-weakening friction property. The friction parameters a, b, critical distance, and effective normal stress of the nonuniform friction model are shown in Figure 3. Below 4km depth, the a-b equals -0.0015 (weakly velocity weakening) over the conditionally stable zone, while a-b equals to -0.004 (strongly velocity weakening) over two asperities (Figure 3c and 3f). The effective normal stress on the conditionally stable zone is 50 MPa and over two asperities Z1 and Z2 is 90 MPa (80% higher than the conditionally stable zone) and 70 MPa (40% higher than the conditionally stable zone) respectively, where Z1 is a high normal stress (HNS) asperity and Z2 is a low normal stress (LNS) asperity. We set up higher normal stress on two asperities to represent two zones of topographic high, for example subducted seamounts, in the conditionally stable zone. Based on Luo and Duan (2018), the normal stress increase over seamounts is related to the ratio of the seamount height to the seamount basal diameter. A 900m high seamount with a basal diameter of 6 km can increase the normal stress to 80 MPa from 50 MPa in the surrounding area. In this study, we do not explicitly include seamounts into our models. Instead, we set up the elevated normal stress of 90 MPa and 70 MPa over the two asperities to represent two seamounts of different sizes. There are four main models with different combinations of the two velocity models (simple vs heterogeneous) and the two friction models (uniform vs nonuniform) (Table 1). Models 1 and 3 utilize the simple velocity model, while Models 2 and 4 apply the heterogeneous velocity model.

202

203

204

205

206

207

208

209

210

211

212

213

214

215

216

217

218

219

220

221

222

Models 1 and 2 utilize the uniform friction model on the fault plane, while Models 3 and 4 utilize the nonuniform friction model. Previous studies find that fluid overpressurization could give rise to low effective normal stress along subduction zones (Kitajima & Saffer, 2012; Bassett *et al.*, 2014; Kimura *et al.*, 2012) and we build Model 5 with low effective normal stress to examine its effect. Model 5 uses the heterogeneous velocity model and the nonuniform friction model, similar to Model 4. The main difference comes from the low effective normal stress on the conditionally stable zone (30 MPa) and on two asperities (42 MPa, 40% higher than conditionally stable zone) (Figure S1). In Model 5, the average normal stress over the whole fault plane is lower than that in Models 1-4 (~60%).

We calculate the h* value for all models based on equation (3) (Figure S2 and S3). In this study, h* is used as a reference to determine whether the fault plane is unstable (H>h*) or conditionally stable (H=<h*). In the uniform friction model, the fault width is much larger than the h* over the fault plane, where earthquakes can both nucleate and propagate (Figure S2). In the nonuniform friction model, the size of asperities is large than h* on them and earthquake could nucleate and propagate on them while the width of conditionally stable zone is smaller than h* on it, so that earthquakes cannot nucleate but can propagate on it. In addition, h* is not only related with friction parameters (a, b, σ and L), but also related with shear modulus μ (μ = ρ * V_s ²), thus h* for the hanging wall and footwall might be different in the heterogeneous velocity model, shown in Figure S2 and S3.

4. Results

4.1 Earthquake cycles

245

246

247

248

249

250

251

252

253

254

255

256

257

258

259

260

261

262

263

264

265

266

We briefly present earthquake cycle results of the five models here to set the stage for discussing dynamic events to compare roles of fault friction and upper-plate velocity structure. Given the computational challenge of this type of 3D dynamic modeling discussed earlier, we only simulate three earthquake cycles that include at least three dynamic events for each model (Figure 4). We find that the normal stress, which may be considered as a fault plane property as it determines the fault frictional strength (together with the frictional coefficient), plays an important role in determining the recurrence interval. The smallest interval of ~100 years comes from Model 5 (~100 Years) with low normal stress of 30 MPa on the conditionally stable zone and 42 MPa on the asperities. For Model 1 and Model 2, the recurrence intervals are around 160 years due to a higher initial normal stress of 50 MPa over the fault plane (no asperities). The longest interval of ~220 years occurs in Model 4, where normal stress is 50 MPa on the conditionally stable zone, 90 MPa on HNS asperity Z1 and 70 MPa on LNS asperity Z2. Another important result here is that the more compliant upper-plate material at shallow depth (Figure 1c) appears to facilitate cascading failures of multiple asperities over the whole fault plane, as can been seen by comparing dynamic events in Models 4 and Model 3 (Table 1 and Figure 4). Every dynamic event in Model 4 with the more compliant upper-plate material ruptures both asperities, while most of dynamic events in Model 3 only ruptures one of the two asperities. We calculate the h* value based on the depth dependent velocity structure and the two-layer structure, and find that the low velocity at shallow depth leads to a low rigidity and a smaller h* at shallow depth, shown in Figure S3, which contributes to more unstable failure in Model 4.

4.2 Rupture speeds

Historical tsunami earthquakes are well known for their unusual slow rupture speeds, typically lower than 1.5 km/s (Pelayo and Wiens, 1992; Ammon $et\,al.$, 2006; Lay $et\,al.$, 2011). In this study, we quantitatively calculate the rupture speed for all models to evaluate which factor contributes more to the slow rupture speed. We select the first dynamic event (D1) in each model to plot their rupture time contours, where the rupture time (t_r) is determined by the time when slip rate first reaches the threshold of v_l = 0.01 m/s at each fault node during the dynamic rupture process (Figure 5). Based on the rupture time, we calculate the rupture speed as inverse of rupture slowness (Bizzarri & Das, 2012):

$$v_r(x_s, x_d) = \frac{1}{\|\nabla_{(x_s, x_d)} t_r(x_s, x_d)\|}$$
 (4)

where x_s and x_d are along strike and along dip directions. Because the rupture speed near earthquake nucleation point could be extremely low, we exclude those areas during rupture speed calculation (Figure 5). In addition, we select two along dip (depth) bands to obtain two profiles showing how rupture speed changes at different depth (Figure 5), with one profile closer to the nucleation point (red line) and the other further away (black line), to compare with depth-dependent velocity structure.

Generally, the rupture speed is limited to be lower than *Vs* of the hanging wall at each depth, shown in Figure 5. We compare the rupture speeds in Models 1 and 2 to explore the influence from the upper plate property (Figures 5a and 5b). We find that the rupture speed at shallow depth (<10 km) in Model 2 is lower than that in Model 1, because the velocity in the hanging wall is lower in Model 2 than in Model 1 at shallow depth. In Model 2, rupture speed at depth of 1-3km drops to 1.5-2.0 km/s, though still higher than typical tsunami earthquake rupture speed <1.5 km/s and the

narrow range (1-3 km) is not consistent with the depth range of historic tsunami earthquakes (<10 km). At the topmost layer (<1km depth), the rupture front encounters the free surface and the rupture speed accelerates to be supershear, larger than Vs in the hanging wall. We use rupture speed results in Models 3-5 to study the influence from the fault property (Figure 5c-e), because these models all utilize the nonuniform friction model, with two strongly velocity weakening asperities embedded in the conditionally stable zone. The rupture speed over the asperities is still high (2-3km/s), while the rupture speed in the conditionally stable zone effectively drops to be lower than 1.5 km/s, unrelated with depth. The topmost layer (<1km depth) still has some scattered segments of supershear rupture speed. However, supershear zones are not continuous along the trench and are separated by very low rupture speed zones updip of the central conditionally stable zone. Comparing Models 3 and 4, rupture speed over the conditionally stable zone in Model 4 is slightly faster than that in Model 3, which could be related to a more compliant hanging wall and smaller h* in Model 4, shown in Figure S3, making the fault more unstable. In Model 5, the low normal stress on the asperities and the conditionally stable zone further contributes to slowing down the rupture speed, comparing with that in Model 4.

288

289

290

291

292

293

294

295

296

297

298

299

300

301

302

303

304

305

306

307

308

309

We try to calculate the average rupture speed over multiple dynamic events (for example, D1-D3) in each model, in order to better estimate the rupture speed over earthquake cycles. Unlike the first dynamic event D1 nucleating from the left side of the fault plane for all models (Figure 5), the earthquake nucleation points may change for later dynamic events (D2-D3), making it difficult to compare average rupture speed. We compare the average rupture speed for Models 1-5 in Figure S4 along the red profile of Figure 5. The average speed over the conditionally stable zone stays stable at around 1.5 km/s or below at all depth (Models 3-5). The average speed for Model 1 is around 2.5-

3km/s along the profile, while it drops to 2-2.5 km/s (close to 2 km/s) in Model 2. It supports that a more compliant upper plate reduces rupture speed to some extent, though not enough to 1.5 km/s or lower.

313

314

315

316

317

318

319

320

321

322

323

324

325

326

327

328

329

310

311

312

4.3 Stress change, slip, moment rate

We compare the stress change, final slip and moment rate function for the first dynamic event of each model in Figure 6. The maximum stress drop and slip come from Models 1 and 2, both of which have strongly velocity weakening friction over the fault plane. The maximum final slip is especially high near shallow depth for Model 2 (~16 m), while the maximum final slip for Model 1 is ~12.5 m. This phenomenon is due to the more complaint hanging wall velocity structure in Model 2, consistent with the previous study (Prada et al., 2021). The two models have similar average stress drops (~5.1 MPa) and similar total moments (~1.0*10²¹Nm, ~Mw 7.9), which are much higher than those in Models 3-5. Models 3-5 have two separate velocity weakening asperities embedded in the conditionally stable zone. The stress drop and slip are higher near two asperities, while lower in the conditionally stable zone, demonstrating that the conditionally stable zone contributes not only to slow rupture speed but also to low stress drop and final slip. The average stress drops in Models 3 and 4 are \sim 3.0 MPa and the total moments are also close, 4.06*10²⁰ Nm (Mw 7.68) from Model 3 and 4.49*10²⁰ Nm (Mw 7.71) from Model 4. In Model 5, the average stress drop significantly reduces to ~1.65 MPa due to the low normal stress condition, leading to smaller final slip (maximum 3.5 m) and total moment (2.3* 10^{20} Nm, ~ Mw 7.5).

To better study stress drop over a sequence of earthquakes over multiple earthquake cycles, we calculate the average stress drops over the whole fault plane, inside asperities and outside asperities (over the conditionally stable zone), for all dynamic events simulated in Models 1-5, shown in Figure S5. Although the stress drop values may scatter among the different dynamic events in each model, it is still obvious that low normal stress in Model 5 contributes to the low average stress drop compared with other models. In Models 3-5, stress drop on the conditionally stable zone is much lower than that on the asperities, due to the weakly velocity weakening friction property and low normal stress in the conditionally stable zone. The average stress drop values are also listed in Table 1.

4.4 Normalized moment rate and spectrum

Because the simulated events have different moments, we use the earthquake scaling relations (Kanamori and Anderson, 1975; Vidale and Houston, 1993) to normalize the moment rate functions by following Houston *et al.* (1998) and Bilek and Lay (1999) to remove effects of the total moment on the shape of the moment rate function, shown in Figure 7. The normalization can be expressed as

346
$$\dot{M}_{norm}(t) = \left(\frac{M_{0ref}}{M_0}\right)^{\frac{2}{3}} \dot{M}(\tau), \quad t = \left(\frac{M_{0ref}}{M_0}\right)^{\frac{1}{3}} \tau$$
 (5),

where τ is the original time, t is the normalized time, M_0 is the total moment of the event, M_{0ref} is the seismic moment of a reference earthquake (Mw 6 used in this study), $\dot{M}(\tau)$ is the original moment rate function and $\dot{M}_{norm}(t)$ is the normalized moment rate function.

To avoid overestimation of source duration due to the low moment rate at the early and late stages of a simulated event, we use a threshold of moment rate $> 10^{17}$ Nm/s, about the moment rate of a M_w 5.5 earthquake, to determine the starting and ending times in $\dot{M}(\tau)$ for source duration measurements (Figure 6). The source duration of the normalized moment rate function is defined as the normalized duration for the event. We measure the normalized durations of all simulated events as listed in Table 1 and Figure S6 and compare them with those observed from historical tsunami earthquakes. The normalized duration of observed historical tsunami earthquakes ranges from 9 to 23 s (Table S1), much larger than deeper megathrust earthquakes of around 5 s (Bilek and Lay, 2002). The simulated events in Models 3 and 5 of this study have larger normalized durations (> 10s) than those from other models, primarily due to the low rupture speed in the conditionally stable zone. For Model 5 (low normal stress), the exceptionally long normalized duration (e.g., 14 s for D2) is further related with the low normal stress. The normalized duration is proportional to duration and cube root of moment, $T/M_0^{1/3}$. A low normal stress leads to a lower total moment M_0 . Therefore, a slightly longer source duration T, shown in Figure S7, leads to a significantly longer normalized duration in this event. However, the events simulated in Model 2 (compliant upper plate) only have slightly increased normalized durations compared to those in Model 1. This is because the compliant upper plate mainly slows down the ruptures at 1-3 km depth with minor effects on the deeper part of the subduction plane. In addition, the normalized duration in Model 4 is shorter than in Model 3 due to the influence of the compliant upper plate in Model 4. As discussed earlier, dynamic events tend to rupture a series of asperities more smoothly in a cascade fashion with a faster rupture speed due to the compliant upper plate.

350

351

352

353

354

355

356

357

358

359

360

361

362

363

364

365

366

367

368

369

Based on the normalized moment rate functions, we calculate and compare the spectrum of all simulated events D1, shown in Figure 8. In Models 3-5, the spectra have much lower corner frequency (where moment starts to decrease) and are more depleted of high frequency energy compared with spectrum in Model 1, under the influence of nonuniform friction. Such phenomena are consistent with common features of historical tsunami earthquakes. However, for Model 2, the corner frequency is nearly the same with that in Model 1, implying a very weak effect on corner frequency reduction from the compliant upper plate.

4.5 Moment-scaled radiated energy

Previous studies found that historical tsunami earthquakes have lower moment-scaled radiated energy compared with other subduction zone interplate and intraplate earthquakes (Lay et al., 2012; Meng et al., 2015). Thus, in this study, we calculate moment-scaled radiated energy for the simulated dynamic events in Models 1-5 to compare with the observed values. Based on analysis of the slip-stress history on each point over the fault plane, we are able to calculate the radiated energy (E_R) for each dynamic event, by subtracting the estimated dissipated static energy (W_{static}) from the total strain energy (W_{total}), shown by the equation below (Ma and Archuleta, 2006; Ide, 2002).

387
$$E_R = W_{total} - W_{static} = \int_{\Sigma} \frac{\sigma_0(\xi) + \sigma_1(\xi)}{2} \cdot \Delta u_1(\xi) d\Sigma - \int_0^{\infty} \int_{\Sigma} \sigma(\xi, t) \cdot \Delta v(\xi, t) d\Sigma dt$$
 (6)

where $\sigma_0(\xi)$ is the initial stress, $\sigma_1(\xi)$ is the final stress, $\sigma(\xi, t)$ is the stress during faulting, $\Delta u_1(\xi)$ is the final slip and $\Delta v(\xi, t)$ is the slip rate during the faulting.

The calculated radiated energy density for D1 event in Model 1 and in Model 5 are shown in Figures 9 and 10. We find that radiated energy is positive for most of the velocity weakening zone

in Model 1 and for two velocity weakening asperities in Model 5. However, most of the area in the conditionally stable zone in Model 5 has negative radiated energy, which serves as an energy sink that will significantly reduce the total radiated energy and further reduce the moment-scaled radiated energy value, because the slip in the conditionally stable zone still significantly contributes to the total moment. In the conditionally stable zone, the initial shear stress is only slightly larger than the final shear stress (small stress drop), which implies that the strain energy could be much lower than the dissipated energy, which generates a negative radiate energy in this zone (Figure 10c).

We compare the moment-scaled radiated energy for D1 event in all models (1-5) with the observed subduction zone earthquakes in Figure 11. We find the scaled energy values are highest for Models 1 and 2, near the upper bound of values for the interplate earthquakes, and lower for Models 3 and 4, below the lower bound of values for the interplate earthquakes, due to the energy sink effect of the conditionally stable zone. Comparing Model 5 with Model 4, we find that a lower effective normal stress will further reduce the moment-scaled radiated energy to a value close to historical tsunami earthquakes. We further estimate the average moment-scaled energy through earthquake cycles for all models, using average radiated energy dividing with average moment in each model, shown in Figure S8. The average values slightly differ from event D1, but the general trend is similar, supporting the contribution coming from both the heterogeneous friction and low effective normal stress. In fact, considering the computational efficiency, we limit the fault dimensions for Models 1-5 (~80 km) shorter along strike than historical large tsunami earthquakes (>100km). We expect a further reduction of scaled energy in Models 3-5, if we use a longer fault plane with a larger area of the conditionally stable zone to serve as energy sinks.

4.6 Simulated seafloor displacement from Model 5

414

415 In this section, we present simulated seafloor displacement from event D2 (Mw 7.5, normalized 416 duration of 14 s) of Model 5, shown in Figure 12ab. This Mw 7.5 event with a centroid depth near 417 10 km causes permanent vertical ground surface displacement up to 1m and horizontal displacement 418 more than 2 m. Large seafloor displacement occurs over a large area of 70 km (along trench) by 30 419 km (perpendicular to trench). An observed tsunami earthquake with similar magnitude and centroid 420 depth is the 1996 Peru Mw 7.5 event, which led to tsunami runups of several meters (5 meter in 421 maximum) along a coastline near Peru, though the maximum recorded wave heights are only tens of centimeters on tide gauges in the Pacific ocean (Ihmle et al., 1998; Heinrich et al., 1998). This 422 423 historical event demonstrates that tsunami earthquakes could occur as deep as 10 km and cause 424 unneglectable tsunami hazard. We plot the continuous waveforms of seafloor displacement for 425 stations within a virtual array located over the hanging wall (Figure 12c). The displacement 426 waveforms are complex and the stations to the left side (X< 0 km) show two displacement runup 427 stages. This complexity is related with the noncontinuous rupture of multiple asperities in the 428 nonuniform friction model. In addition, we find that two stations (A and B) near the trench have 429 larger displacement than other near trench stations (Figure 12c). Based on the final slip distribution 430 over fault plane (Figure S7), two places on the subduction plane below stations A and B have larger 431 slip than other near trench area. From the rupture speed distribution (Figure S9), a strong variation 432 of rupture speed occurs along strike at shallow depth, with high speed (supershear, > 2km/s) near 433 stations A and B and low speed (<<1 km/s) between stations A and B. This results in a low average rupture speed from station A to station B of below 1 km/s (Figure S10), despite that the rupture 434 435 speed near station A and B locally exceeds shear wave velocity. In fact, these places (near stations

A and B) of high rupture speed, large final slip and large seafloor displacement locate updip of the two asperities.

438

439

440

441

442

443

444

445

446

447

448

449

450

451

452

453

454

455

456

436

437

5. Discussion

In this study, we explore whether the upper-plate velocity structure or the fault friction is more important in tsunami earthquake generation and characteristics. We find that in the models with the nonuniform friction distribution, the conditionally stable zone can effectively slow down rupture speed to be lower than 1.5 km/s (typical tsunami earthquake rupture speeds), no matter what velocity structure is used. Correspondingly, the nonuniform friction distribution also contributes to long normalized duration, low corner frequency, high frequency energy depletion and low momentscaled radiated energy, consistent with the features observed from historical tsunami earthquakes. The heterogeneous upper-plate velocity structure is not sufficient to slow down the rupture speed to be <1.5 km/s even at very shallow depth (<3 km), when the uniform friction distribution is applied on the main fault plane (Model 2). Furthermore, the normalized duration elongation, corner frequency reduction, high frequency energy depletion effects and low moment-scaled radiated energy are all neglectable in this model. The most significant contribution from the heterogeneous upper-plate velocity structure is the enhancement of slip near trench, as shown in comparison between Models 1 and 2. Generally, the factors of strong velocity weakening, high normal stress and compliant upper plate in Model 2 contribute to large moment release and large final slip near trench, which could generate large seafloor displacement and fatal tsunami waves. On the contrary, the factors of conditionally stable zone, low normal stress and compliant upper plate in Model 5

contribute to slow rupture speed, slow moment release rate, depletion of high frequency energy and enhanced slip near shallow depth. We propose tsunami earthquakes more likely occur in subduction zones with on-fault property and upper-plate property similar to Models 3-5. With nonuniform friction, slow rupture speed and small slip occur in a conditionally stable zone, while fast rupture speed and large slip mainly occur on asperities, forming multiple moment rate release peaks. In addition, discontinuous supershear rupture may occur near trench updip of asperities, but average rupture speed along the trench could be much lower, due to rupture slowing down effect from the conditionally stable zone. Low normal stress further contributes to slow moment release rate and exceptionally long normalized duration. Compliant hanging wall promotes cascade failure of multiple asperities to generate larger tsunami earthquakes and enhances shallow slip, thus increasing the tsunami potential.

In Model 5, the overall normal stress is lower than other models and could generate earthquakes with lower stress drops, longer normalized duration and low moment-scaled energy, consistent with observed features of historical tsunami earthquakes. Complex moment rate functions caused by asperities have been widely observed in tsunami earthquakes and numerous shallow subduction zone earthquakes (Bilek *et al.*, 2004). An overall low effective normal stress could make the fault plane more heterogeneous. For example, if the average effective normal stress is 20 MPa in the conditionally stable zone, then a patch with higher normal stress of 50 MPa (30 MPa higher) will reduce h* on it to be 40% of that in the surrounding area and thus becomes more unstable, assuming all other parameters in equation (3) a - b, L, μ are the same. On the other hand, if the effective normal stress is 100MPa in the conditionally stable zone, then a patch with normal stress of 130 MPa (still 30 MPa higher) only reduces h* to be about 77% compared with the surrounding area.

This may help explain why the source time functions of shallow subduction zone earthquakes, including tsunami earthquakes, are more complex compared with deeper earthquakes (Bilek *et al.*, 2004).

479

480

481

482

483

484

485

486

487

488

489

490

491

492

493

494

495

496

497

498

499

500

In our models, we mainly compare the influence of heterogeneous fault friction and heterogeneous upper-plate velocity structure on tsunami earthquake generation and characteristics. Limited by computation needs of dynamic earthquake cycle simulations, we do not explore parameter spaces in detail by varying friction parameters (e.g., a-b value and L), changing fault geometry/dimension or varying location of asperities. For example, if we separate two asperities further away in Models 3, 4 and 5 using a longer fault dimension, the normalized duration for the simulated events could be longer and become more comparable to the observed range of 9-23 s of historical tsunami earthquakes, as demonstrated by Meng et al. (2022). The general slow rupture speed of <1.5 km/s in the conditionally stable zone is a proof of this possibility. In a longer fault plane with a larger conditionally stable zone as energy sink, the moment-scaled radiated anergy could be further reduced. A typical tsunami earthquake may form by rupturing a series of critically stressed asperities embedded over a long conditionally stable zone, for example 100-200 km along strike. However, there is no key difference in physics for shallow subduction zone earthquakes of shorter or longer dimensions, as illustrated by Bilek and Lay (2002). In this study, we use weakly velocity weakening of a-b=-0.0015 in the conditionally stable zone in the non-uniform friction models. If we set different friction parameters of even less velocity weakening in the conditionally stable zone, the rupture speed might be further slowed down. In addition, the asperity depths are all around 10 km for Models 3-5 and the simulated tsunami earthquakes have a centroid depth of 10 km, which generates smaller near-trench fault slip and seafloor displacement, for example 1-2

meters in amplitude in Model 5. If we set up asperities shallower, for example < 5km depth, we could expect much larger near-trench fault slip and seafloor displacement. We remark that, in addition to fault friction and upper-plate elastic properties, other factors such as the potential plastic yielding in the accretionary prism may also slow down rupture propagation and generate large seafloor displacement (Ma, 2012; Ma and Kirakawa, 2013). In the future, other potentially important factors should also be considered and systematically compared when studying specific tsunami earthquakes or over specific subduction zones.

6. Conclusions

In this study, we systematically compare contributions of heterogeneous fault friction and heterogeneous upper plate properties to tsunami earthquake generation and characteristics. Heterogeneous upper-plate properties are not sufficient to slow down ruptures to typical tsunami earthquake speed of <1.5 km/s over a large depth range (< 10 km). In contrast, heterogeneous fault friction distributions with asperities embedded in a conditionally stable zone can significantly slow down rupture speeds to be <1.5 km/s in the conditionally stable zone and generate long duration moment rate functions involving complex peaks, with spectra of low corner frequency, depleted high frequency energy and lower moment-scaled radiated energy. In addition, low effective normal stress on the subduction plane facilitates generating earthquakes with low stress drops, long normalized durations and small radiated energy, consistent with the observed features of tsunami earthquakes. The depth dependent velocity structure with low rigidity at shallow depth mainly enhances large slip near trench and promotes cascading ruptures of multiple asperities in the conditionally stable zone. Tsunami earthquakes can happen at a centroid depth of 10 km, generating seafloor displacement with non-neglectable tsunami hazard. Our results show that heterogeneous

523 fault friction provides a suitable environment for tsunami earthquake generation over a wide range of depth, playing a more important role than heterogeneous elastic property in tsunami earthquake 524 525 characteristics. 526 527 Acknowledgements 528 This research is supported by NSF grants EAR-2013695 and EAR-2147340. The authors thank the 529 Editor and two anonymous reviewers for their constructive comments that improve the manuscript. 530 authors also appreciate Texas A&M High Performance Research Computing 531 (https://hprc.tamu.edu) for providing the advanced computer resources used in this study. 532 533 **References:** 534 Abercrombie, R. E., M. Antolik, K. Felzer, and G. Ekström (2001), The 1994 Java tsunami earthquake: 535 106, 6595-6607, Slip subducting seamount, Geophys. Res., 536 doi:10.1029/2000JB900403. 537 Ammon, C. J., H. Kanamori, T. Lay, and A. A. Velasco (2006), The 17 July 2006 Java tsunami earthquake, 538 Geophys. Res. Lett., 33, L24308, doi:10.1029/2006GL028005. 539 Bassett, D., Sutherland, R. & Henrys, S. (2014), Slow wavespeeds and fluid overpressure in a region of

Bilek, S. L., and E. R. Engdahl (2007), Rupture characterization and aftershock relocations for the 1994

shallow geodetic locking and slow slip, Hikurangi subduction margin, New Zealand. Earth

540

541

542

Planet. Sci. Lett. 389, 1-13.

543	and 2006 tsunami earthquakes in the Java subduction zone, Geophys. Res. Lett., 34, L20311,					
544	doi:10.1029/2007GL031357.					
545	Bilek, S.L., Lay, T. (1999). Rigidity variations with depth along interplate megathrust faults in subduction					
546	zones. Nature 400, 443–446 doi:10.1038/22739					
547	Bilek, S.L., Lay, T. (2002), Tsunami earthquakes possibly widespread manifestations of frictional					
548	conditional stability. Geophysical Research Letters 29, 18-1-18-4 doi:10.1029/2002gl015215					
549	Bilek, S.L., Lay, T., Ruff, L.J., 2004. Radiated seismic energy and earthquake source duration variations					
550	from teleseismic source time functions for shallow subduction zone thrust earthquakes. Journal					
551	of Geophysical Research 109, n/a–n/a doi:10.1029/2004jb003039					
552	Bizzarri, A., & Das, S. (2012). Mechanics of 3-D shear cracks between Rayleigh and shear wave rupture					
553	speeds. Earth and Planetary Science Letters, 357-358, 397-404.					
554	https://doi.org/10.1016/j.epsl.2012.09.053					
555	Chen, T., and N. Lapusta (2009), Scaling of small repeating earthquakes explained by interaction of					
556	seismic and aseismic slip in a rate and state fault model, J. Geophys. Res. Solid Earth, 114(B1),					
557	doi:10.1029/2008JB005749.					
558	Contreras-Reyes, E., Maksymowicz, A., Lange, D., Grevemeyer, I., Muñoz-Linford, P., & Moscoso, E.					
559	(2017). On the relationship between structure, morphology and large coseismic slip: A case					
560	study of the Mw 8.8 Maule, Chile 2010 earthquake. Earth and Planetary Science Letters, 478,					
561	27–39. https://doi.org/10.1016/j.epsl.2017.08.028					
562	Dieterich, J.H., Richards-Dinger, K.B., 2010. Earthquake Recurrence in Simulated Fault Systems, in: .					

563	pp. 233–250 doi:10.1007/978-3-0346-0500-7_15.
564	Duan, B. (2010), Role of initial stress rotations in rupture dynamics and ground motion: A case study
565	with implications for the Wenchuan earthquake, J. Geophys. Res. Solid Earth, 115(B5),
566	doi:10.1029/2009JB006750.
567	Duan, B. (2012), Dynamic rupture of the 2011 Mw 9.0 Tohoku-Oki earthquake: Roles of a possible
568	subducting seamount, J. Geophys. Res., 117(B5), doi:10.1029/2011JB009124.
569	Duan, B., and S. M. Day (2008), Inelastic strain distribution and seismic radiation from rupture of a fault
570	kink, J. Geophys. Res., 113(B12), doi:10.1029/2008JB005847.
571	Duan, B., and D. D. Oglesby (2006), Heterogeneous fa 734 ult stresses from previous earthquakes and

573 doi:10.1029/2005JB004138. 574 Heinrich, P., Schindele, F., Guibourg, S., Ihmlé, P.F., 1998. modeling of the February 1996 Peruvian 575 Tsunami. Geophysical Research Letters 25, 2687–2690.. doi:10.1029/98gl01780

the effect on dynamics of parallel strike-slip faults, J. Geophys. Res., 111(B5),

572

576

577

578

579

580

581

582

Houston, H., H. M. Benz, and J. E. Vidale, Time functions of deep earth- quakes from broadband and short period stacks, J. Geophys. Res., 103, 29,895–29,913, 1998.

Hughes, T. J. (2000), The Finite Element Method: Linear Static and Dynamic Finite Element Analysis, Courier Corporation.

Hyndman, R. D., Yamano, M., & Oleskevich, D. A. (1997). The seismogenic zone of subduction thrust faults. Island Arc, 6(3), 244-260.

Hyndman, R. D., & Wang, K. (1993). Thermal constraints on the zone of major thrust earthquake failure:

583	The Cascadia subduction zone. Journal of Geophysical Research: Solid Earth, 98(B2), 2039-
584	2060.
585	Ide, S. (2002), Estimation of radiated energy of finite-source earthquake models, <i>Bull. Seismol. Soc.</i>
586	<i>Am.</i> , 92 (8), 2994–3005.
587	Ihmle', P. F., J. M. Gomez, P. Heinrich, and S. Guibourg (1998), The 1996 Peru tsunamigenic earthquake:
588	Broadband source process, Geophys. Res. Lett., 25, 2691–2694.
589	Kanamori, H. (1972), Mechanism of tsunami earthquakes, Phys. Earth Planet. Inter., 6, 346-359,
590	doi:10.1016/0031-9201(72)90058-1.
591	Kanamori, H., & Anderson, L. (1975). Theoretical basis of some empirical relations in
592	seismology. Bulletin of the Seismological Society of America, 65, 1073–1095.
593	Kanamori, H., and M. Kikuchi (1993), The 1992 Nicaragua earthquake: A slow tsunami earthquake
594	associated with subducted sediments, Nature, 361, 714-716, doi:10.1038/361714a0.
595	Kitajima, H. & Saffer, D. M. (2012), Elevated pore pressure and anomalously low stress in regions of
596	low frequency earthquakes along the Nankai Trough. Geophys. Res. Lett. 39, L23301.
597	Kimura, G., S. Hina, Y. Hamada, J. Kameda, T. Tsuji, M. Kinoshita, and A. Yamaguchi (2012), Runaway
598	slip to the trench due to rupture of highly pressurized megathrust beneath the middle trench
599	slope: The tsunamigenesis of the 2011 Tohoku earthquake off the east coast of northern Japan,
600	Earth Planet. Sci. Lett., 339–340, 32–45, doi:10.1016/j.epsl.2012.04.002
601	Kuo, ST., Duan, B., and Meng, Q. (2022). Comparing roles of fault friction and upper-plate rigidity in
602	depth-dependent rupture characteristics of megathrust

603	earthquakes. https://doi.org/10.1002/essoar.10511621.1
604	Lapusta, N., and Y. Liu (2009), Three-dimensional boundary integral modeling of spontaneous
605	earthquake sequences and aseismic slip, J. Geophys. Res. Solid Earth, 114(B9).
606	doi:10.1029/2008JB005934.
607	Lapusta, N., Rice, J. R., Ben-Zion, Y., & Zheng, G. (2000). Elastodynamic analysis for slow tectonic
608	loading with spontaneous rupture episodes on faults with rate- and state-dependent friction.
609	Journal of Geophysical Research: Solid Earth, 105(B10), 23765-23789.
610	https://doi.org/10.1029/2000jb900250
611	Lay, T., Ammon, C. J., Kanamori, H., Yamazaki, Y., Cheung, K. F., & Hutko, A. R. (2011). The 25
612	October 2010 Mentawai tsunami earthquake (Mw7.8) and the tsunami hazard presented by
613	shallow megathrust ruptures. <i>Geophysical Research Letters</i> , 38(6), n/a-n/a.
614	https://doi.org/10.1029/2010gl046552
615	Lay, T., Kanamori, H., Ammon, C.J., Koper, K.D., Hutko, A.R., Ye, L., Yue, H., Rushing, T.M. (2012),
616	Depth-varying rupture properties of subduction zone megathrust faults. Journal of Geophysical
617	Research: Atmospheres 117, n/a–n/a doi:10.1029/2011jb009133
610	Liu D. and B. Duan (2018). Scanario Forthquaka and Ground Motion Simulations in North China

Liu, D., and B. Duan (2018), Scenario Earthquake and Ground-Motion Simulations in North China:
 Effects of Heterogeneous Fault Stress and 3D Basin Structure, Bull. Seismol. Soc. Am.,
 doi:10.1785/0120170374.

621

622

Liu, Y., Rice, J.R. (2007). Spontaneous and triggered aseismic deformation transients in a subduction fault model. Journal of Geophysical Research 112.. doi:10.1029/2007jb004930

623	Luo, B., and B. Duan (2018), Dynamics of Non-planar Thrust Faults Governed by Various Friction Laws,					
624	J. Geophys. Res. Solid Earth, doi:10.1029/2017JB015320.					
625	Luo, B., Duan, B., and Liu, D. (2020), 3D Finite-Element Modeling of Dynamic Rupture and Aseisr					
626	Slip over Earthquake Cycles on Geometrically Complex Faults. Bulletin of the Seismologica					
627	Society of America, 110, 2619–2637, doi:10.1785/0120200047.					
628	Ma, S., Archuleta, R.J. (2006), Radiated seismic energy based on dynamic rupture models of faulting.					
629	Journal of Geophysical Research: Atmospheres 111, n/a–n/a doi:10.1029/2005jb004055					
630	Ma, S. (2012). A self-consistent mechanism for slow dynamic deformation and tsunami generation for					
631	earthquakes in the shallow subduction zone. Geophysical Research Letters, 39(11), L11310.					
632	Ma, S., and Hirakawa, E. T. (2013), Dynamic wedge failure reveals anomalous energy radiation of					
633	shallow subduction earthquakes. Earth and Planetary Science Letters, 375, 113-122.					
634	Meng, Q., Heeszel, D.S., Ye, L., Lay, T., Wiens, D.A., Jia, M., Cummins, P.R. (2015), The 3 May 2006					
635	(Mw8.0) and 19 March 2009 (Mw7.6) Tonga earthquakes: Intraslab compressional faulting					
636	below the megathrust. Journal of Geophysical Research: Solid Earth 120, 6297-6316					
637	doi:10.1002/2015jb012242					
638	Meng, Q., Duan, B., Luo, B. (2022). Using a dynamic earthquake simulator to explore tsunami					
639	earthquake generation. Geophysical Journal International 229, 255–273					
640	doi:10.1093/gji/ggab470					
641	Pelayo, A. M., & Wiens, D. A. (1992). Tsunami earthquakes: Slow thrust-faulting events in the					
642	accretionary wedge. Journal of Geophysical Research, 97(B11).					

643	https://doi.org/10.1029/92jb01305
644	Prada, M., Galvez, P., Ampuero, J. P., Sallarès, V., Sánchez-Linares, C., Macías, J., & Peter, D. (2021).
645	The Influence of Depth-Varying Elastic Properties of the Upper Plate on Megathrust Earthquake
646	Rupture Dynamics and Tsunamigenesis. Journal of Geophysical Research: Solid Earth, 126(11)
647	https://doi.org/10.1029/2021jb022328
648	Qiang, S. (1988), An adaptive dynamic relaxation method for nonlinear problems, Computers
649	&Structures, 30(4), 855-859.
650	Rubin, A.M., and Ampuero, JP. (2005). Earthquake nucleation on (aging) rate and state faults. Journal
651	of Geophysical Research: Atmospheres 110 doi:10.1029/2005jb003686.
652	Saffer, D.M., Lockner, D.A., Mckiernan, A., 2012. Effects of smectite to illite transformation on the
653	frictional strength and sliding stability of intact marine mudstones. Geophysical Research
654	Letters 39, n/a–n/a doi:10.1029/2012gl051761
655	Sallares, V., & Ranero, C. R. (2019). Upper-plate rigidity determines depth-varying rupture behaviour of
656	megathrust earthquakes. Nature, 576(7785), 96-101. https://doi.org/10.1038/s41586-019-1784-
657	$\underline{0}$
658	Scholz, C. H. (1998), Earthquakes and friction laws, Nature 391:37-42.
659	Vidale, J.E., Houston, H. (1993). The depth dependence of earthquake duration and implications for
660	rupture mechanisms. Nature 365, 45–47 doi:10.1038/365045a0
661	Wang, C. (1980). Sediment subduction and frictional sliding in a subduction zone. Geology, 8(11),

530–533.

Tables and Figures

665

Table 1. Models 1-5 and their simulated dynamic event results

Models (friction & velocity)	Dynamic Phases (Ruptured asperities)	Slip weighted Stress Drop (MPa)	Normalized duration (s)	Mw
Model 1	D1	5.1	4.7	7.94
(simple velocity model & uniform friction	D2	3.0	7.3	7.61
model)	D3	4.6	5.8	7.89
Model 2	D1	5.2	4.5	7.97
(heterogeneous velocity model & uniform	D2	3.0	7.7	7.67
friction model)	D3	3.0	6.7	7.78
Model 3	D1 (Z1Z2)	2.9	9.8	7.68
(simple velocity model & nonuniform friction	D2 (Z2)	2.6	11.6	7.32
model)	D3 (Z1)	3.0	8.4	7.58
	D4 (Z2)	2.4	13.3	7.30
Model 4	D1 (Z1Z2)	3.0	7.7	7.71
(heterogeneous velocity model & nonuniform	D2 (Z1Z2)	3.1	7.2	7.74
friction)	D3 (Z1Z2)	3.0	7.2	7.73
Model 5	D1 (Z1Z2)	1.7	10.6	7.51
(heterogeneous velocity model & nonuniform	D2 (Z1Z2)	1.6	14.0	7.51
riction with low normal stress)	D3 (Z1Z2)	1.6	10.6	7.52

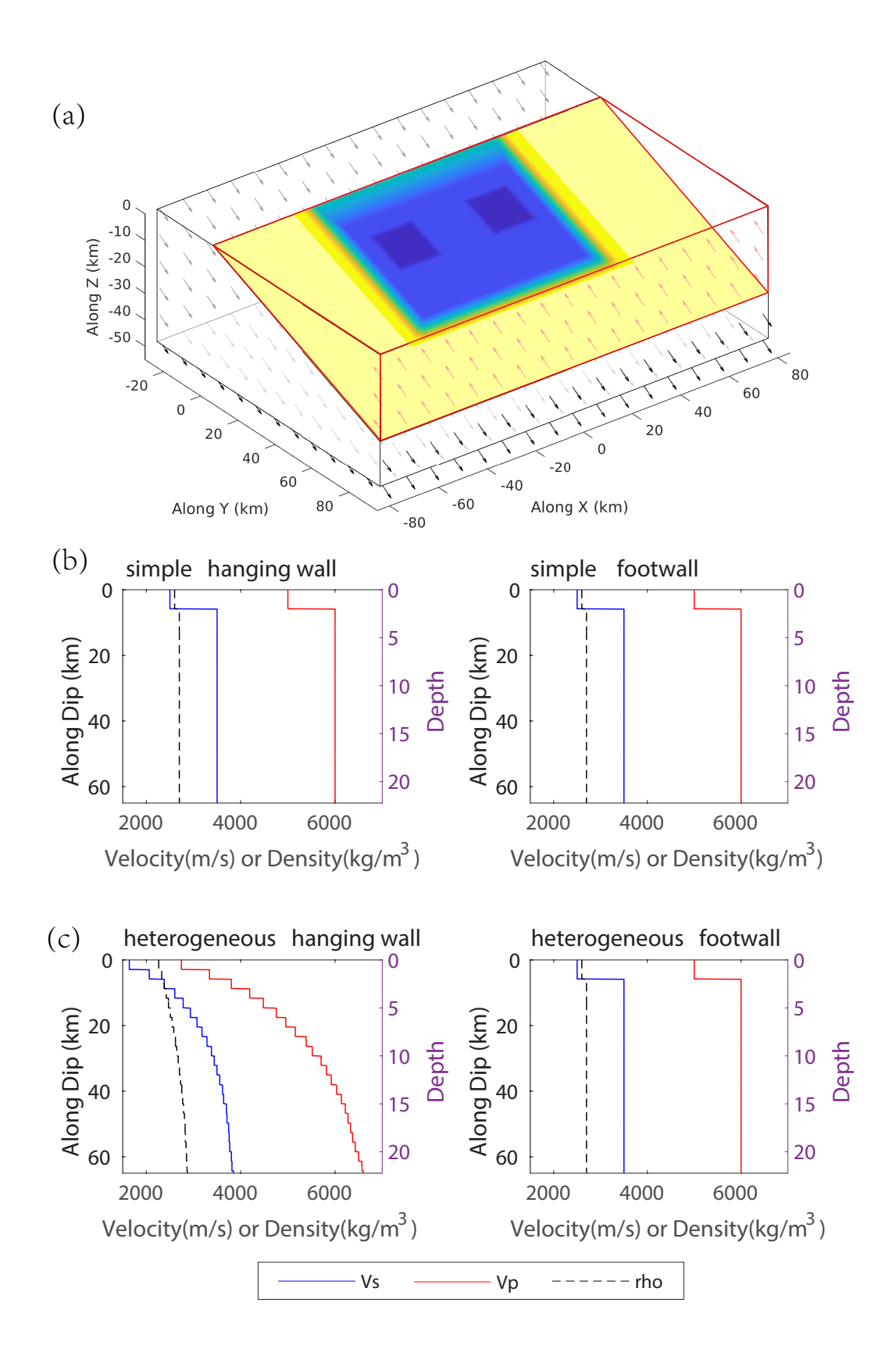


Figure 1. (a) Schematic diagram for fault geometry (a 20° dipping subduction plane) and boundary conditions of the models, with dimension of the model along *X* axis: Xmin (-80km) to Xmax (80km),

along Y axis: Ymin (-30 km) to Ymax (80 km) and along Z axis: Zmin (-50 km) to Zmax (0 km). The main fault plane (blue) with a largely velocity-weakening frictional property that can host earthquake ruptures is surrounded by a velocity-strengthening area (yellow) that creeps. During the quasi-static phase, one half of the plate convergence rate (0.5*10°9m/s) parallel with the fault plane is applied upward (red arrows at the boundary Y=Ymax) on hanging wall (outlined by red frame) and downward (black arrows at boundaries Y=Ymax, Y=Ymin and Z=Zmin) on footwall wall (outlined by black frame). (b) The simple velocity model that both the hanging wall and footwall use the same two-layer velocity structure, where Vp=5.0 km/s and Vs=2.5km/s at the top layer (<2km) and Vp=6.0km/s and Vs=3.5km/s at the bottom layer. (c) Heterogeneous velocity model that the hanging wall uses a depth varying velocity structure (Sallares and Ranero, 2019) with low velocity near shallow depth, where Vp=2.7 km/s and Vs=1.6 km/s near the trench, and the footwall uses a two-layer velocity structure as the simple velocity model, shown in (b).

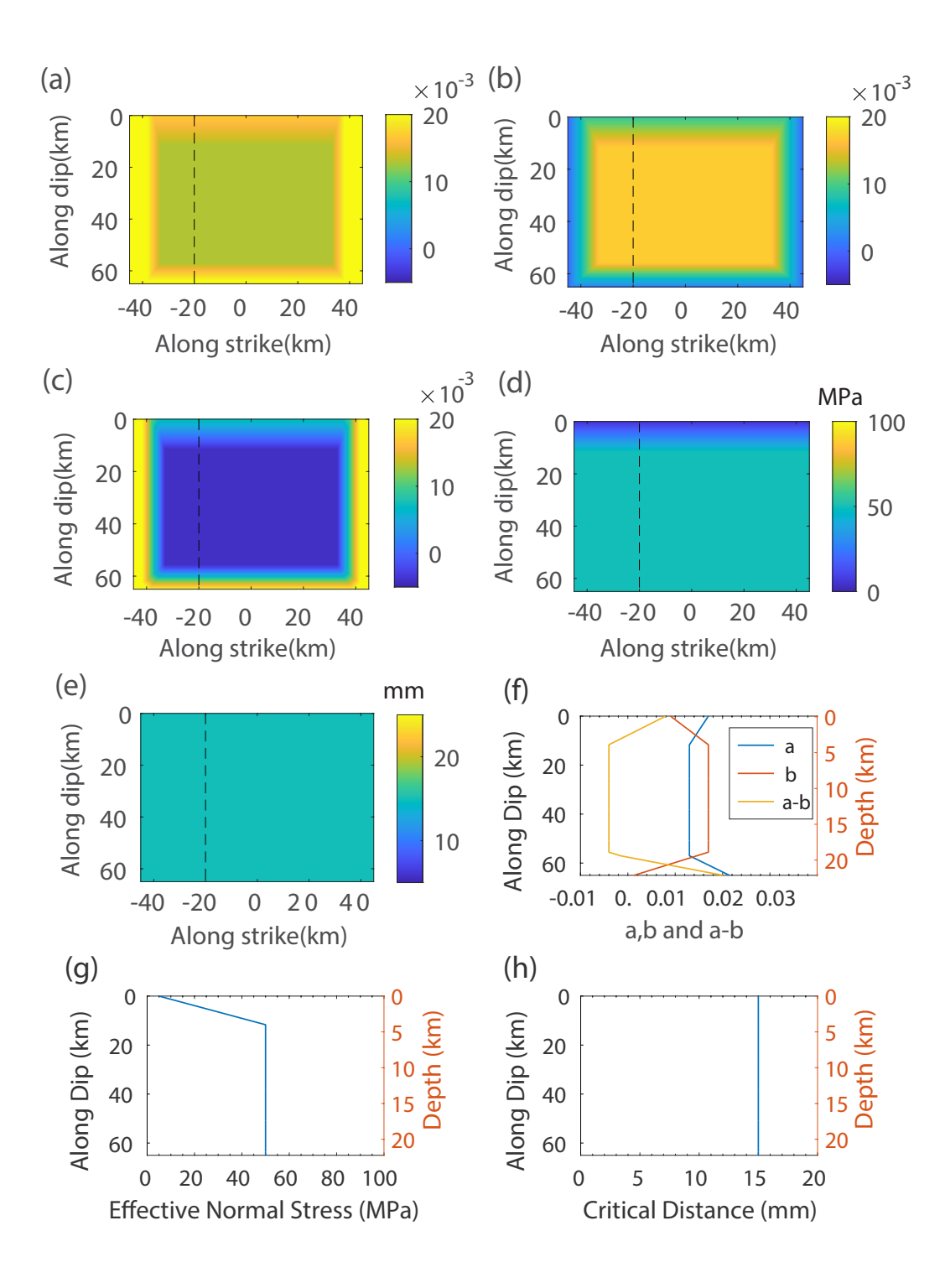


Figure 2. The on-fault parameters for the uniform friction model (in Models 1 and 2): distributions of friction parameters (a) a, (b) b, (c) a-b, (d) effective normal stress and (e) critical distance over the fault plane; the cross sections of friction parameters (f) a, b, a-b, (g) effective normal stress, and (h) critical distance along a dip profile (the dashed lines in (a)-(e)). The fault is velocity

strengthening near the trench (a-b=0.008 at 0km depth) and quickly transitions to velocity weakening (a-b=-0.004 at depth =4 km) and stay uniform over most of the fault plane, then transitions to velocity strengthening at bottom of the main fault plane (a-b=0.02), as shown in (f). The effective normal stress near trench (depth 0 km) is 5MPa and linearly increases to 50 MPa at depth of 4km and keeps uniform over most of the fault plane, as shown in (g).

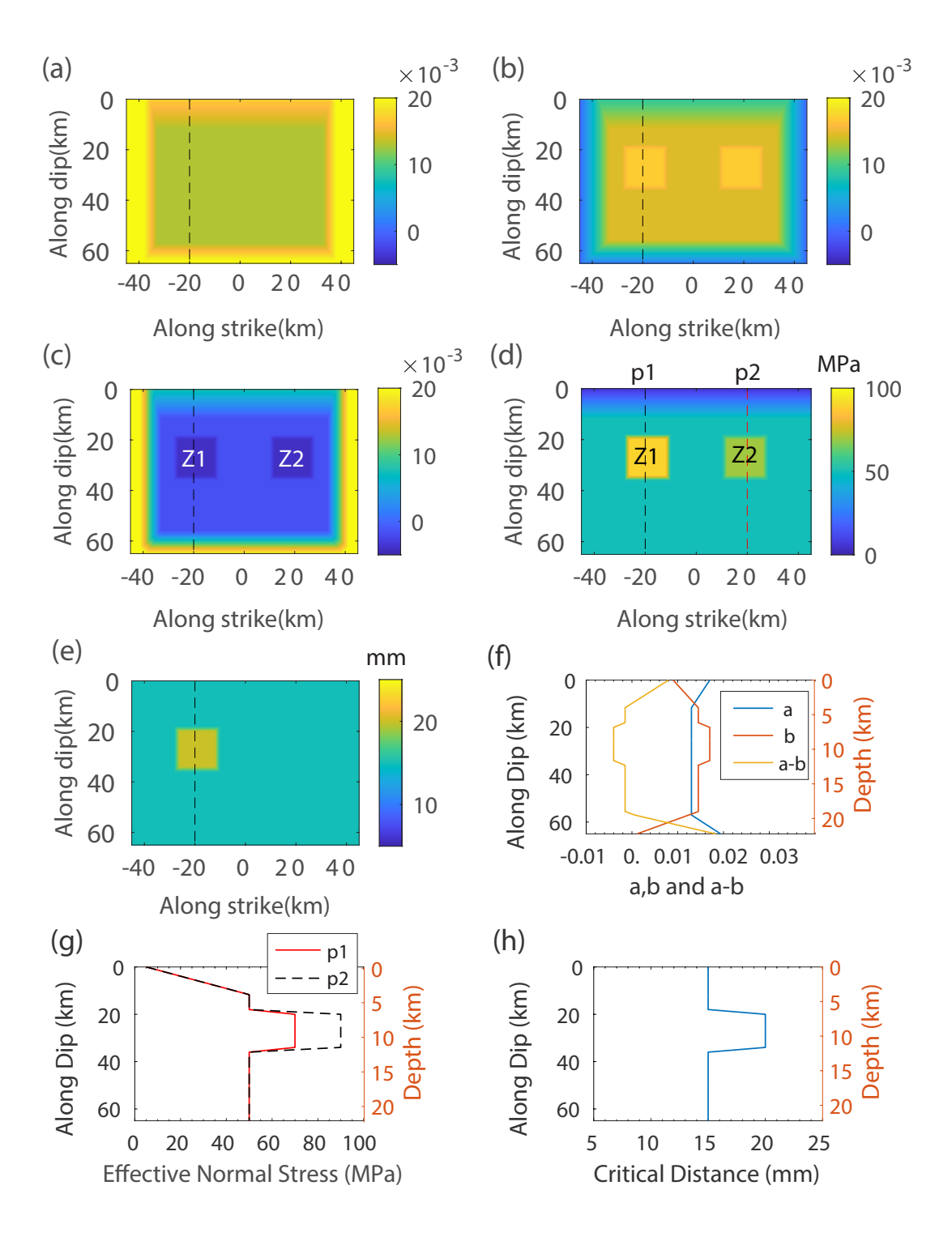


Figure 3. The on-fault parameters for the nonuniform friction model (in Models 3 and 4): distributions of friction parameters (a) a, (b) b, (c) a-b, (d) effective normal stress and (e) critical distance over the fault plane; the cross sections of friction parameters (f) a, b, a-b, (g) effective normal stress, and (h) critical distance along a dip profile (the dashed lines in (a)-(e)). The two

normal stress cross sections p1 and p2 in (g) pass through two asperities Z1 and Z2 shown in (d). The fault is velocity strengthening near the trench (a-b=0.008 at 0km depth) and quickly transitions to conditionally stable (a-b=-0.0015 at depth =4 km) and stay uniform over most of the fault plane below 4 km, then transitions to velocity strengthening at bottom of the main fault plane (a-b=0.02), as shown in (f). On two asperities Z1 and Z2, the a-b equals -0.004 and represents strongly velocity weakening friction property. The effective normal stress near trench (depth 0 km) is 5MPa and linearly changes to 50 MPa at depth of 4km and keeps uniform over most of the fault plane, as shown in (g). On asperity Z1 normal stress is 90 MPa and on Z2 is 70 MPa. Critical distance is 15 mm over most of the fault plane, while on Z1 is 20 mm.

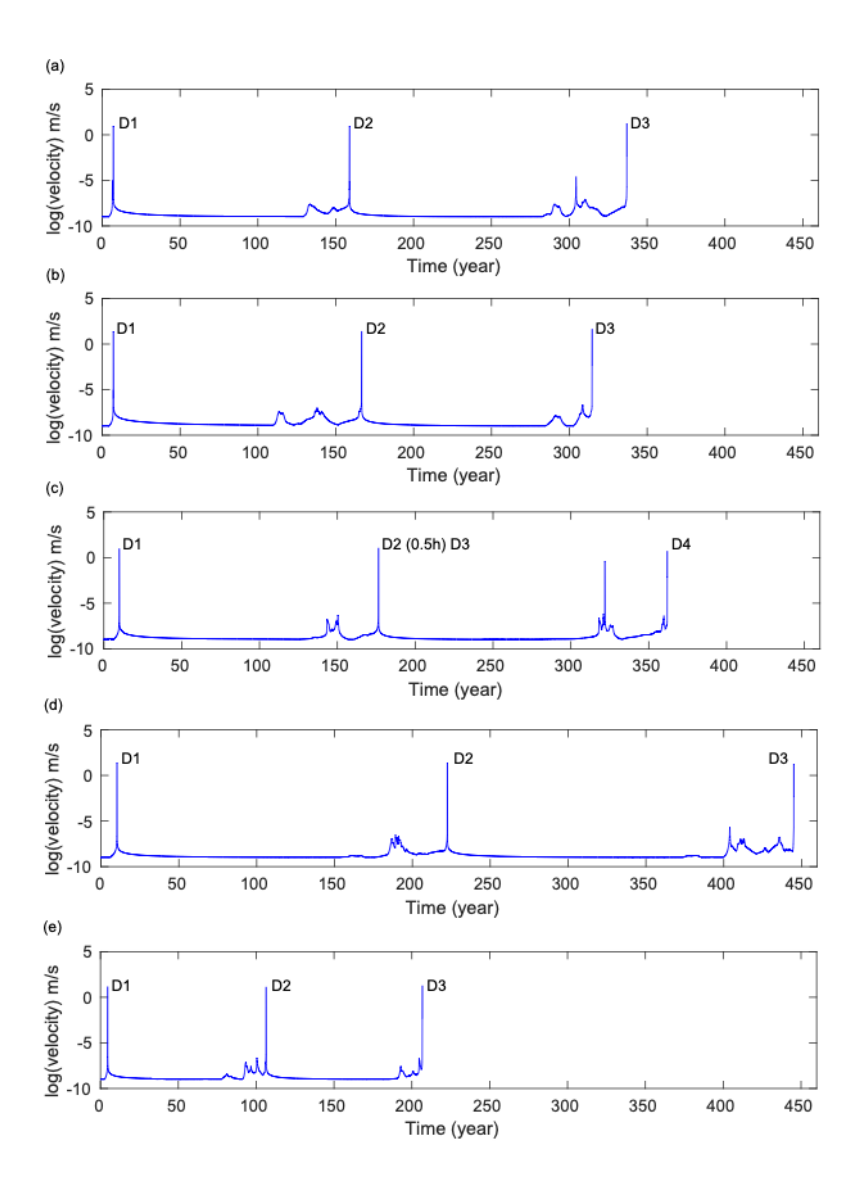


Figure 4. The simulated maximum slip rate on the fault over earthquake cycles, for (a) Model 1, (b) Model 2, (c) Model 3, (d) Model 4, (e) Model 5. The high slip rate peaks (~1 m/s or larger) represent dynamic events and the time (about 100-200 of years) between two dynamic events is the earthquake recurrence interval, except in (c), where two dynamic events (D2 and D3) occurring on the two asperities separately with 0.5 hour delay may be considered as one clusterred event.

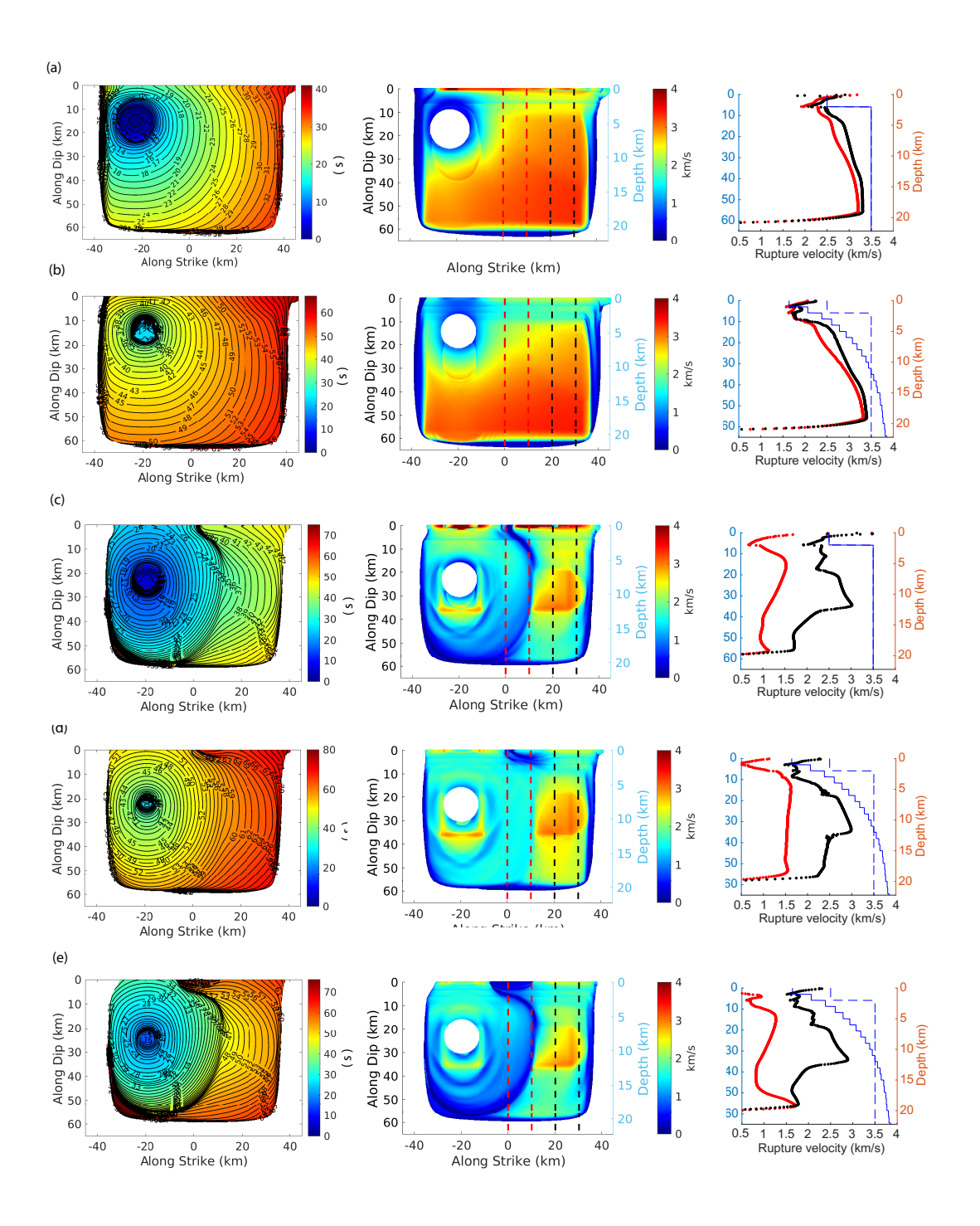


Figure 5. The rupture contour (left column), rupture speed distribution (middle column) and rupture speed profiles (right column), for (a) D1 in Model 1, (b) D1 in Model 2, (c) D1 in Model 3, (d) D1 in Model 4, and (e) D1 in Model 5. For the rupture speed profiles (right column), the red velocity profile shows the average rupture speed of each depth over a narrow zone outlined by two dashed red lines in the rupture speed panels (middle column); and the black velocity profile corresponds to

the average rupture speed within the two black dashed lines in the rupture speed panels (middle column). The blue solid line and dashed line represent the *Vs* velocity of the hanging wall and footwall for comparison.



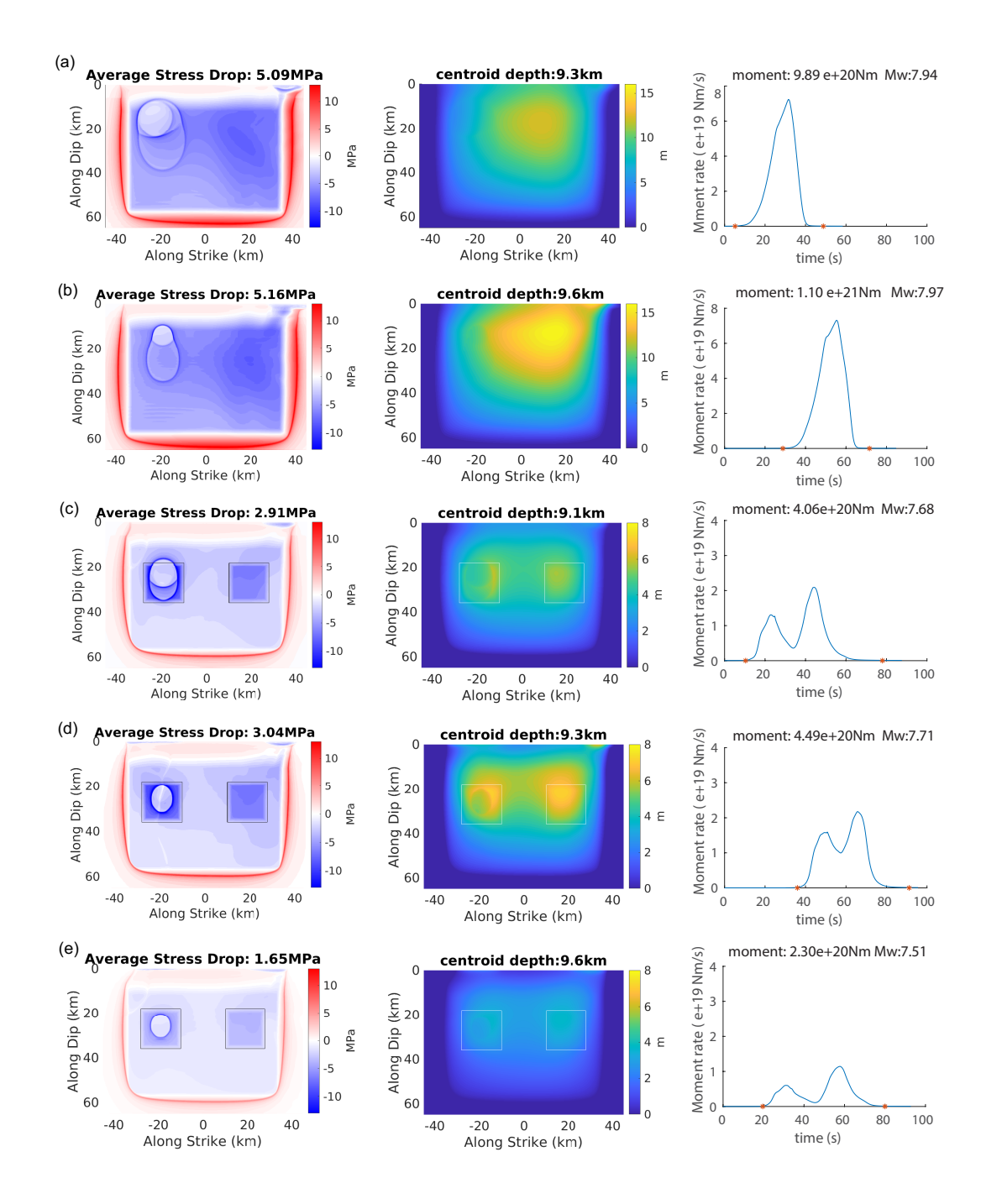


Figure 6. The stress change distribution (left column), final slip distribution (middle column) and

moment rate function, for (a) D1 in Model 1, (b) D1 in Model 2, (c) D1 in Model 3, (d) D1 in Model 4, and (e) D1 in Model 5. The black and white boxes in stress change and final slip panels in (c) (d) (e) represent the locations of two asperities in Models 3-5 with nonuniform friction parameters. The scales of slip and moment rate in (a) (b) are different with those in (c) (d) (e), though the scale of stress changes is the same. Two red stars (10^{17} Nm) on the moment rate functions (right column) denote the starting and ending times used to measure source durations T.



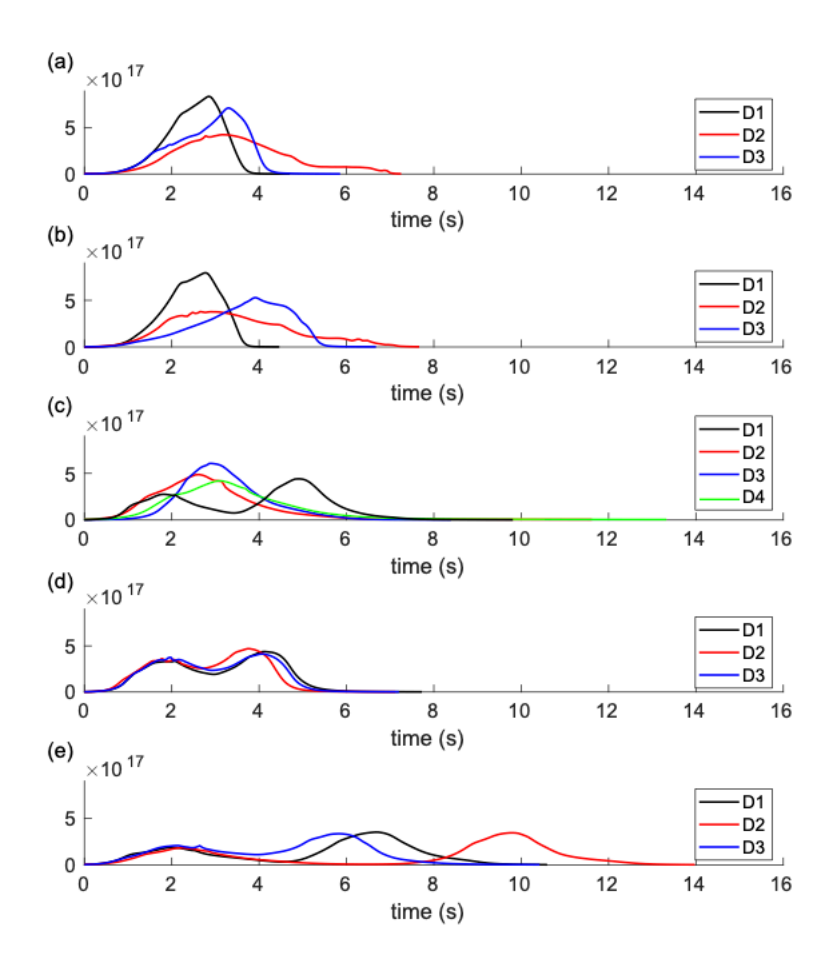


Figure 7. The normalized moment rate functions for all dynamic events simulated in (a) Model 1,

(b) Model 2, (c) Model 3, (d) Model 4, (e) Model 5.

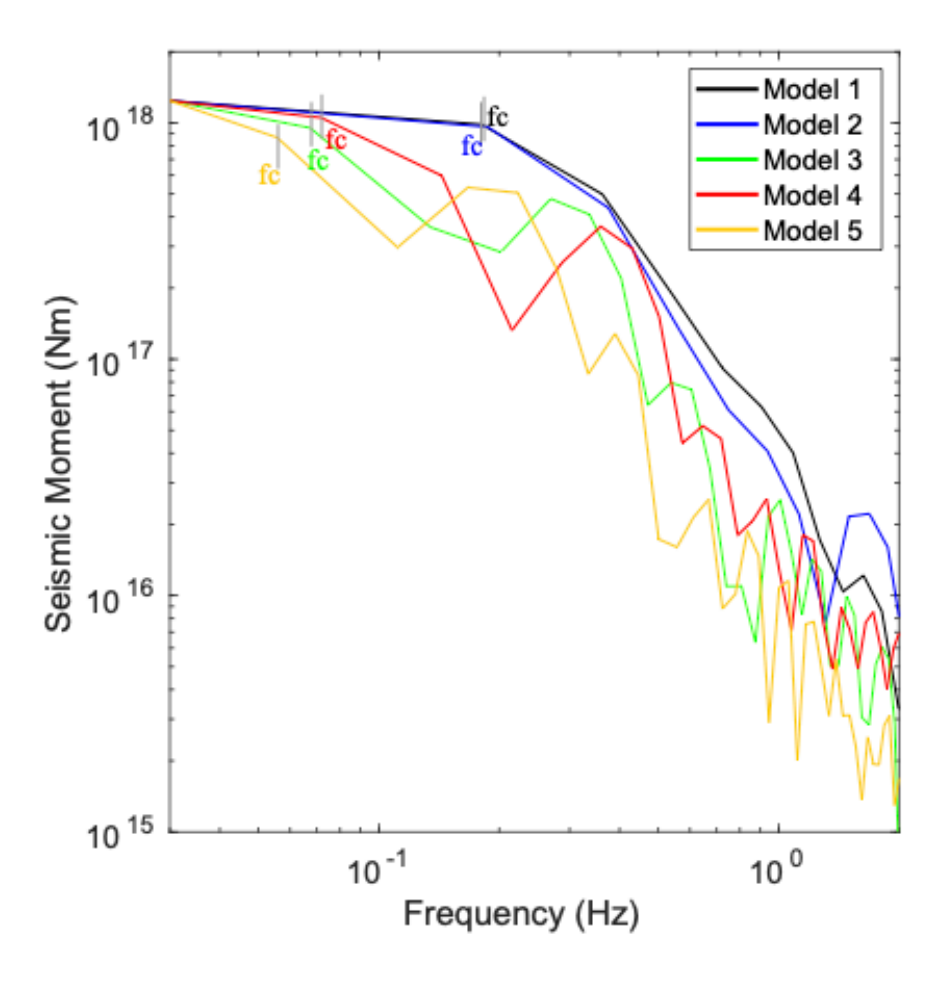


Figure 8. The spectra for the normalized moment rate functions of event D1 in Model 1 (black), Model 2 (blue), Model 3 (green), Model 4 (red) and Model 5 (orange). The normalized moment rate functions are shown in Fig. 7. The vertical bars demonstrate the corner frequencies.

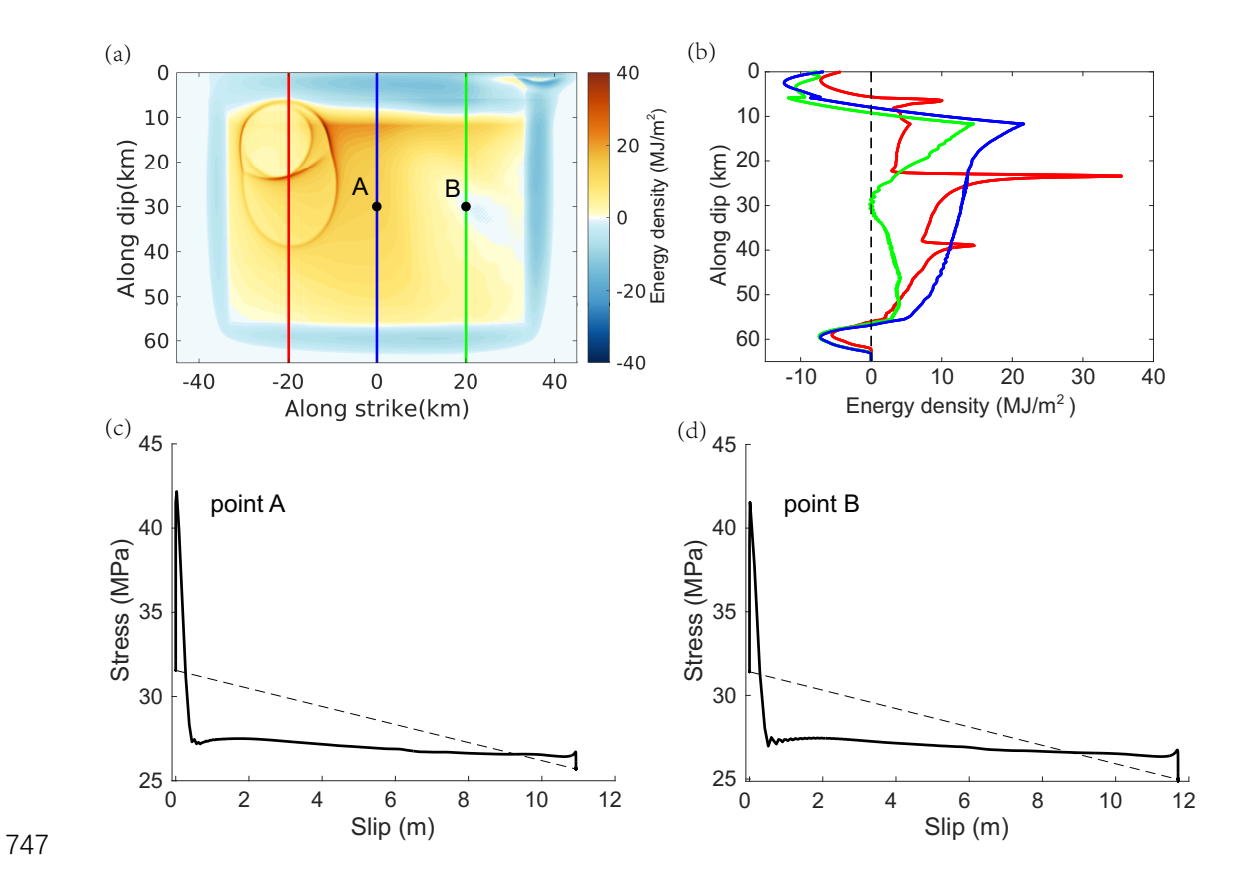


Figure 9. Radiated energy for event D1 in Model 1. (a) Distribution of radiated energy density over fault plane. The radiated energy density is positive over most of the fault plane. (b) Radiated energy density along three profiles shown by red, blue and green lines in (a). (c) Dynamic stress-slip history for point A in (a). The radiated energy is calculated by subtracting the dissipated energy (area below solid line) from the elastic strain energy (area below dashed line). (d) Dynamic stress-slip history for point B in (a).

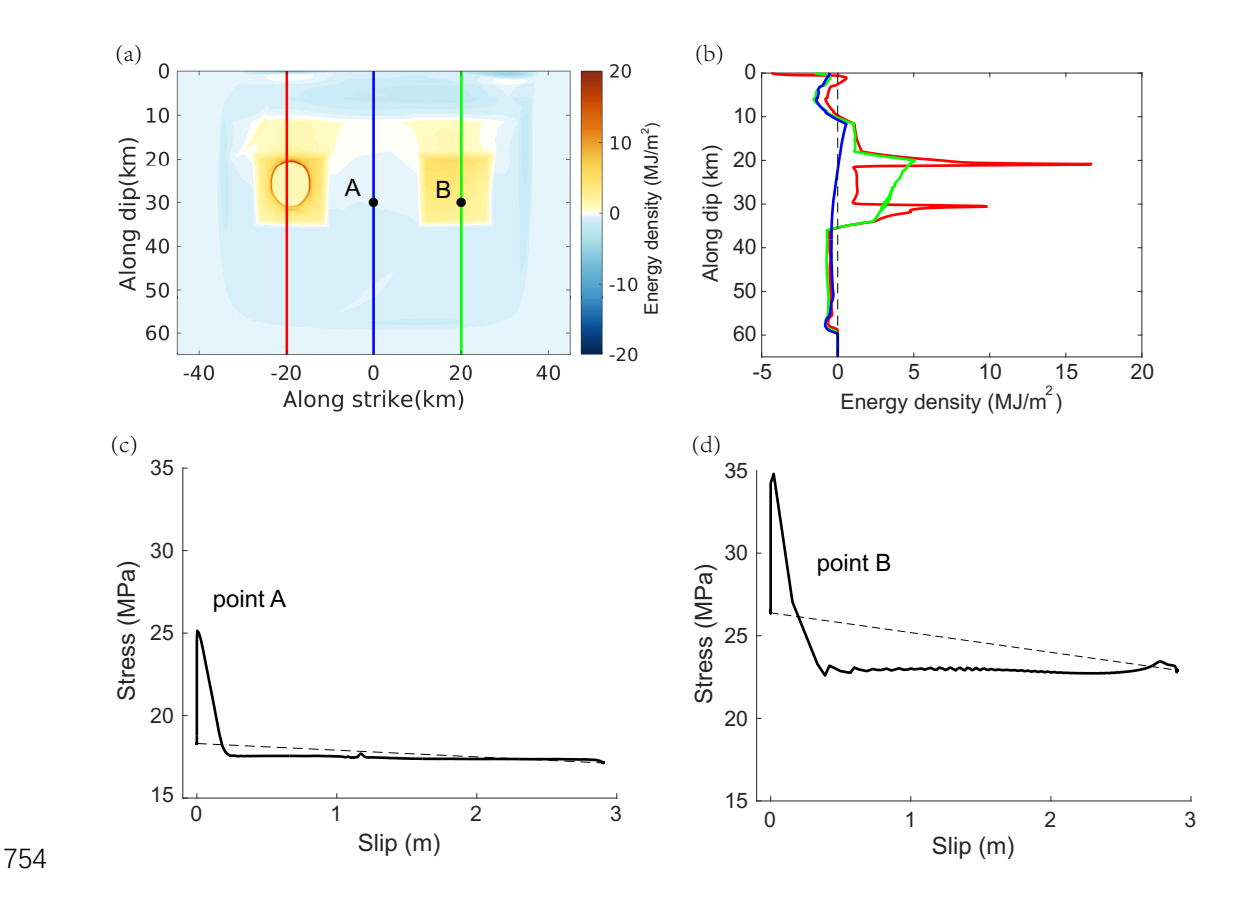


Figure 10. Radiated energy for event D1 in Model 5. (a) Distribution of radiated energy density over fault plane. The positive radiated energy mainly distributes over two asperities. (b) Radiated energy density along three profiles shown by red, blue and green lines in (a). (c) Dynamic stress-slip history for point A in (a). The radiated energy is calculated by subtracting the dissipated energy (area below solid line) from the elastic strain energy (area below dashed line), which obviously results in a negative radiated energy (energy sink) for point A located in the conditionally stable zone. (d) Dynamic slip-stress history for point B in (a), which illustrates a positive radiated energy for point B located on the asperity.

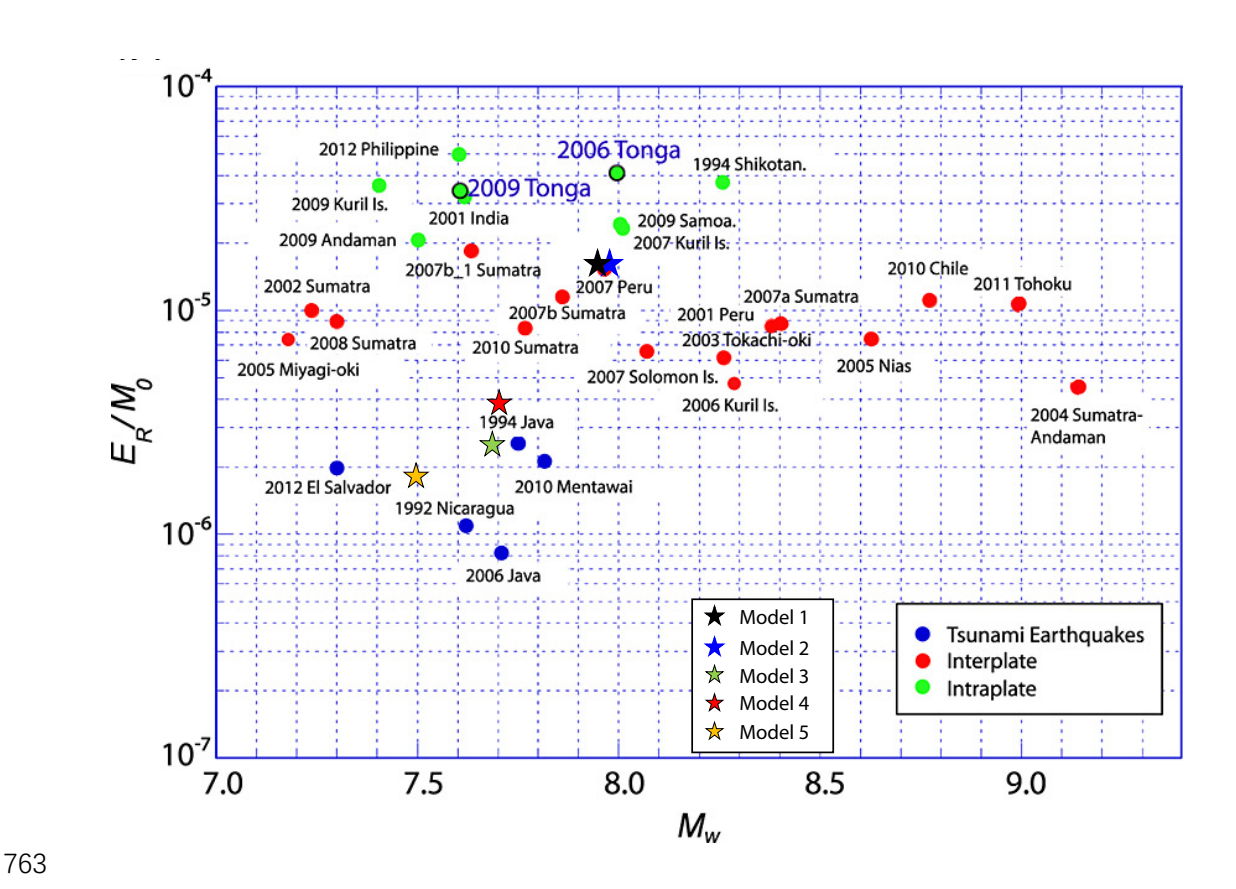


Figure 11. The moment-scaled radiated energy for event D1 in Models 1-5, colored by stars, with values of 1.54·10⁻⁵ for Model 1, 1.55·10⁻⁵ for Model 2, 2.31·10⁻⁶ for Model 3, 3.84·10⁻⁶ for Model 4 and 1.72·10⁻⁶ for Model 5. The colored dots represent the moment scaled radiated energy for historical tsunami, interplate and intraplate earthquakes, from Figure 15c in Meng et al. (2015).

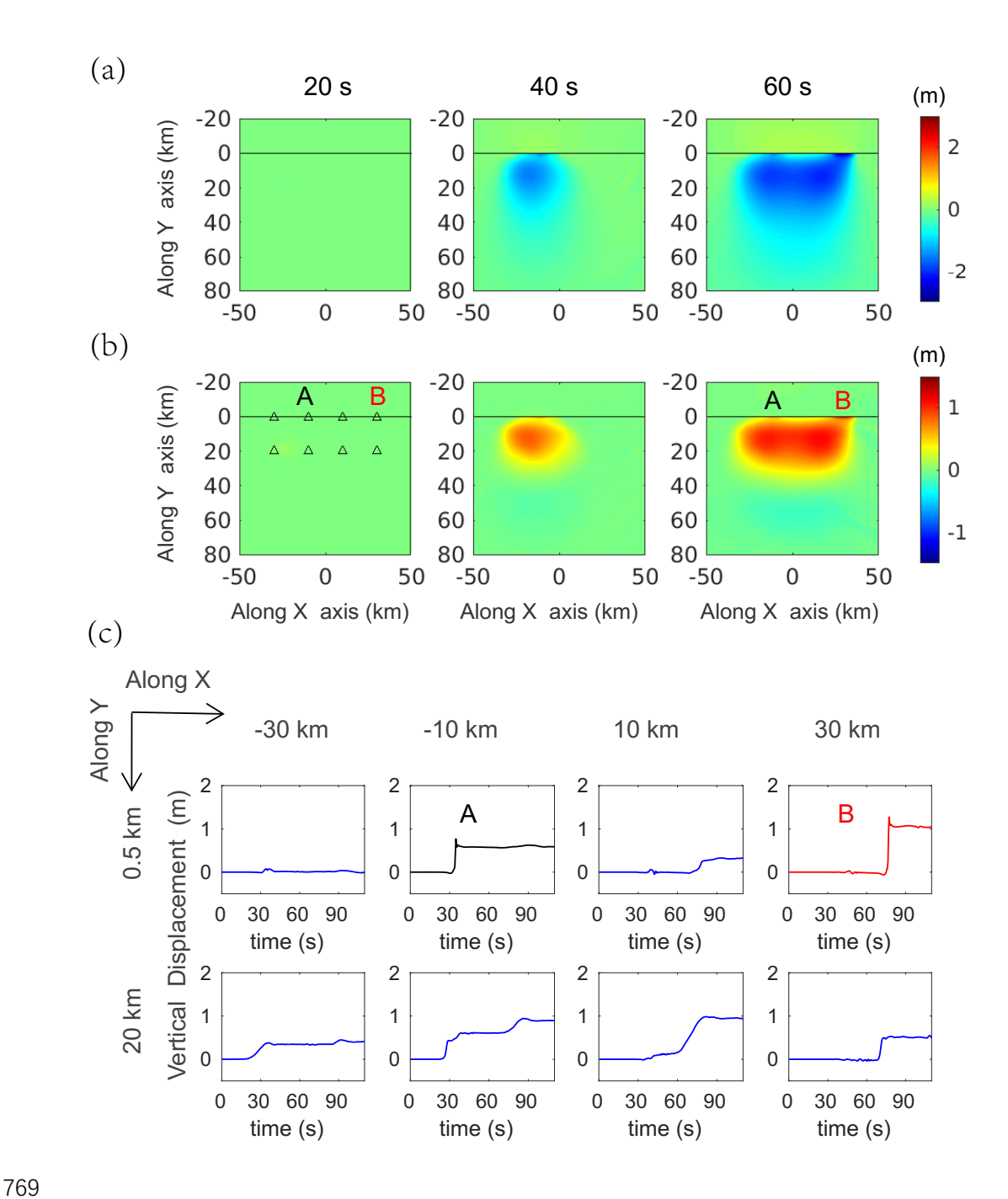


Figure 12. The snapshots of (a) horizontal displacement along Y axis (perpendicular to the trench) and (b) vertical displacement along Z axis at 20s, 60s and 100s of event D2 in Model 5, and (c) time histories of vertical displacement at a virtual array of seafloor stations shown by triangles in (b).